Article:
Bu, X, Lin, G, Shen, X et al. (2 more authors) (2020) Numerical simulation of aircraft thermal anti-icing system based on a tight-coupling method. International Journal of Heat and Mass Transfer, 148. 119061. ISSN 0017-9310

https://doi.org/10.1016/j.ijheatmasstransfer.2019.119061

Numerical Simulation of Aircraft Thermal Anti-icing System Based on a Tight-coupling Method

Xueqin Bu[a], Guiping Lin[a], Xiaobin Shen[a,*], Zhongliang Hu[b], Dongsheng Wen[a,b]

[a] *Laboratory of Fundamental Science on Ergonomics and Environmental Control, School of Aeronautic Science and Engineering, Beihang University, Beijing 100083, China*

[b] *School of Chemical and Processing Engineering, University of Leeds, Leeds LS2 9JT, UK*

Abstract

Considering the influence of surface temperature distribution on air convective heat transfer coefficient, the robust tight-coupling method is firstly developed for aircraft thermal anti-icing simulations under icing conditions. To include the effects of the impinging water droplets on the conjugate heat transfer of thermal anti-icing systems, the Messinger thermodynamic model of runback water film is modified and added to the tightly coupled calculation of the external air flow and the internal solid skin heat conduction. Numerical simulations are carried out on an electro-thermal anti-icing system under both dry air and icing conditions, and the main conclusions below can be drawn. First, convective heat transfer coefficient changes slightly with surface temperature near the leading edge, but is obviously affected by temperature distribution in the downstream area. Second, the anti-icing temperature deviations between the predicted value and the experiment date are acceptable and comparable to the calculation results in the literature, verifying the feasibility and effectiveness of the tight-coupling method. Third, compared with the traditional decoupled loose-coupling method, the robust tight-coupling anti-icing method successfully captures the effect of surface temperature on convective heat transfer coefficient, and predicts higher temperature with lower drop rate on the downstream surfaces.

Keywords: Aircraft icing; Conjugate heat transfer; Tight-coupling method; Electro-thermal anti-icing system; Numerical Simulation

Nomenclature

C_p	specific heat, J/(kgK)
E	total energy, J/kg
f	freezing fraction
h_s	convective heat transfer coefficient, W/(m^{2}K)
h	sensible enthalpy, J/kg
H	thickness of thin virtual wall, m
i	latent heat, J/kg
k	thermal conductivity, W/(mK)
M	molecular weight
$\dot{m}$	mass flow rate, kg/s
t	time, s
T	temperature, K
T_{ad}	reference temperature calculated with adiabatic wall condition, K
T_{ref}	freezing point temperature, 273.15K
T_s	anti-icing surface temperature, also control volume temperature, K
T^f_s	temperature at the interface in the fluid domain, K
T^s_s	temperature at the interface in the solid domain, K
p	pressure, Pa
Pr	Prandtl number
Q	heat flow, W
Q_c	air convective heat flow at the interface, W
Q_n	surface heat flow conducted from internal solid skin, W
S	heat generation rate in a cell of virtual wall, W/m^3
Sc	Schmidt number
S_h	heat source term
u	velocity component, m/s
U	velocity, m/s

x	Cartesian coordinate, m
β	local water droplet collection efficiency
ρ	density, kg/m^3
μ	laminar dynamic viscosity, kg/(ms)
μ_t	turbulent viscosity, kg/(ms)
δ_{ij}	Kronecker delta
Δs	surface area of control volume in virtual wall, m^2

Subscripts

air	air
e	external edge of boundary layer
evap	evaporation
ice	ice
imp	impinging water droplet
in	flowing in
i, j, l	directions in the coordinate
lv	water vaporization
ls	water solidification
out	flowing out
v	vapor
w	water
∞	non-disturbed freestream flow

1. Introduction

Aircraft icing in the air is one of the serious problems that threaten flight safety, and the resulting flight accidents occur from time to time [1]. Generally speaking, aircraft icing refers to the ice accretion on the surfaces of aircraft components caused by the impingement of the super-cooled water droplets in the clouds [2]. This icing damages the aerodynamic shape, increasing aircraft drag and reducing lift and stall angle of attack. Besides, it also causes loss of maneuverability and controllability of the aircraft [3]. To ensure flight safety and meet the requirements of the airworthiness regulations in icing conditions, ice protection systems should be adopted in aircrafts.

At present, bleed air anti-icing system [4] and electro-thermal anti-icing system [5] are the most widely used ice protection strategies. They both heat the aircraft solid skin to raise the surface temperature, preventing ice accumulation in the protected area. As super-cooled water droplets impinge on the heated surface, the collected water, referred to as “runback” when it flows on the surface [6], affects the heat exchange between the external air flow and the internal solid skin. Moreover, the runback water film on the anti-icing surface can change among liquid, solid and vapor phases depending on the heating energy provided [7]. Therefore, simulation of thermal anti-icing systems is a complex multiphase flow, conjugate heat and mass transfer problem with phase change [8]. Current studies always separate the fluid flow and the solid heat conduction into different modules, and perform anti-icing calculation by exchanging interface conditions among different fluid and solid domains. To include the effects of the collected water droplets, heat and mass transfer model of the runback water film on the anti-icing surface, such as Messinger [9], Myers [10] and Shallow water [11], are regarded as an extra module and coupled to the heat exchange of the external air flow and the internal solid skin. The solution methods of the conjugate heat transfer problem can be divided into two types [12]: tight-coupling method (tightly coupled) and loose coupling method (loosely coupled).

With heat conduction code embedded in CFD module, tight-coupling method solves the fluid flow and solid heat conduction equations together at each iteration step, and all the parameters in the computational domains are updated simultaneously. This approach is well understood, and easy to ensure the energy conservations among different domains. The calculation is relatively fast, robust and stable because no further iteration process is required [12]. However, it is difficult for this method to deal with the heat and mass transfer of the runback water film on the anti-icing surface, since the water film module is very different from CFD code. To our best knowledge, the application of the tight-coupling method for the anti-icing simulations under icing conditions has not been reported yet. Hua [13] and Papadakis [14] used tight-coupling methods to analyze the air flow and heat transfer characteristics of bleed air

anti-icing systems under dry air conditions, and the effects of the water droplet impingement and runback water film were not considered. Taking into account the melting process of the accreted ice, Petrosino [15] used a tight-coupling method for the modeling of a coupled bleed air and electro-thermal icing protected system, but the thermodynamics of the impinging water droplets was not simulated either.

Loose-coupling method, on the other hand, solves field equations in each domain individually to provide boundary conditions for adjacent domains. With continuous and iterative exchange of boundary conditions, the calculations in different domains are carried out alternately until the convergence of temperature and heat flux in every interface. This method works as a pure interfacial algorithm, and is completely independent from the details of the solvers and modules of different computational domains [12]. Therefore, it is very easy to couple the water film module and involve the heat fluxes brought by the impingement of the super-cooled water droplets. Moreover, with great flexibility to use any code or any numerical discretization scheme in each domain, the loose-coupling method is thought to be the most efficient and versatile for complex conjugate heat transfer simulations [12]. Currently, almost all the thermal anti-icing studies and software packages, including LEWICE [16]，FENSAP-ICE [17]，ONERA [18]，CANICE [19] and ICECREMO [20], use this method. The iterative procedure of the conjugate heat transfer is expensive, as each domain (especially the fluid domain) could take a considerable amount of time to converge [21, 22]. Therefore, the external air flow is usually decoupled from the conjugate heat transfer solution of the anti-icing system in traditional loose-coupling methods. To stand for the external airflow heat transfer characteristics, the convective heat transfer coefficient is obtained by boundary layer integration methods [23] or CFD methods [24] under isothermal wall boundary conditions, and would not be updated during the coupling iteration of the solid heat conduction and the runback water thermodynamics [22]. However, Morency [25] found that a sharp rise occurred in the convective heat transfer coefficient when non-isothermal temperature increased, and this phenomenon was not captured using constant isothermal surface. With the SST-kω turbulence model of FLUENT software, Domingos [26] found that the convective heat transfer coefficient obtained under the non-isothermal surface boundary condition was much different from that of the isothermal wall in the turbulent region. He also compared the surface temperatures of a hot-air anti-icing system obtained by the coupled and decoupled methodologies of the loose-coupling model, and found that the coupled results were in better agreement with the experimental data [21]. Using the Spalart-Allmaras(S-A) turbulence model of FENSAP-ICE software, Barzi [22] found that the variations in the convective heat transfer coefficients were small with different isothermal surface temperatures, and suggested the decoupled method.

Nevertheless, the surface temperature results changed obviously when the convective heat transfer coefficient was updated during the conjugate heat transfer calculation, indicating that the effect of the non-isothermal temperature distribution should be considered. In addition, Domingos [21] and Barzi [22] both found it took considerably long computational time to simulate the temperature effect on the convective heat transfer coefficient by the loose-coupling method, due to the repetitions of the external flow and internal heat conduction calculations.

To sum up, non-isothermal surface temperature distributions can affect convective heat transfer coefficients, which brings predicted error to the anti-icing simulation. In the loose-coupling method for the anti-icing calculations under icing conditions, it is computationally very expensive to simulate this effect [22]. Therefore, convective heat transfer coefficients are assumed to be independent with surface temperature in the traditional anti-icing simulations. Tight-coupling method automatically updates the convective heat transfer coefficient during the iterative process, but it is difficult to consider the influence of the impinging water on the anti-icing surface. In this paper, the heat flows of the runback water film are added into the tightly coupled calculation of external air flow and internal skin heat conduction by the heat generation rate in the virtual wall of the fluid-solid interface. Then, the tight-coupling method is expanded to simulate the thermal anti-icing systems under icing conditions, and it is robust and efficient for the complex conjugate heat transfer solutions to update convective heat transfer coefficients according to surface temperatures.

2. Tight-Coupling Method and Solution Procedure

2.1. Tight-coupling heat and mass transfer model

The electro-thermal anti-icing system is taken as an example to introduce the tight-coupling heat transfer method, since there are only one interface between the fluid and solid domains in the conjugate heat transfer simulation, making it easy to present the coupling method. For the dry air condition with no water droplets impinging on the anti-icing surface, all the heating energy generated by the electrical heaters within the aircraft skin is taken away by air convection. The external air flow and the internal solid skin domains interact with each other through their interface boundaries, and the equality conditions of the temperature and heat flux at the fluid-solid interface should be ensured as follow [12]:

$$T_s^f = T_s^s \tag{1}$$

$$Q_n = Q_c \tag{2}$$

In the tight-coupling method, with heat conduction solutions embedded in a CFD solver, the energy equations of both solid and fluid domains are established and solved simultaneously, and the heat transfer at the fluid-solid interface can be calculated directly from the solutions in the adjacent cells [27]. In the tightly coupled iteration process, the equality conditions are guaranteed automatically and the convective heat transfer coefficient changes with the interface temperature at each calculation step. However, when super-cooled water droplets are present under icing conditions, they would keep impinging on the anti-icing surfaces. The anti-icing temperature cannot be obtained by just solving fluid-solid conservation equations any more, because a water film would be formed on the anti-icing surface after the droplet impact, and affects the heat transfer characteristics during the processes of runback water flow, evaporation, and freezing. To consider the effects of the impinging water droplets and the water film, the fluid-solid interface of the outer skin surface is set to be an artificial virtual thin wall with one layer of mesh, as shown in Fig. 1. The boundaries of air flow and solid skin domains become the two surfaces of the thin wall.

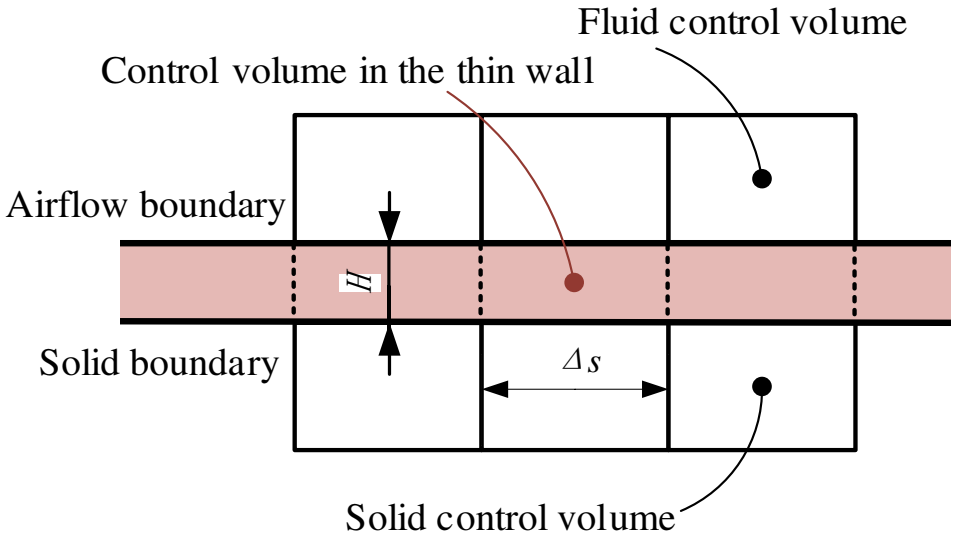

Fig. 1 Artificial virtual thin wall set for the fluid and solid interface.

For the virtual thin wall, only one-dimensional heat conduction equation in the normal direction is established and solved to include an additional thermal resistance. In this situation, Eq. (1) becomes:

$$T_s^f = T_s^s + \frac{Q_n \cdot H}{k \cdot \Delta s} \tag{3}$$

The temperatures at the boundaries of the fluid and solid domains are no longer consistent. However, when the wall has very small thickness and large thermal conductivity, the temperature deviation can be neglected:

$$T_s = T_s^f = T_s^s \tag{4}$$

In addition to the thermal resistance, the virtual wall offers the heat generation rate to model extra heat flow at the fluid-solid interface, and the following equation can be obtained:

$$Q_n + S \cdot H \cdot \Delta s = Q_c \tag{5}$$

It is seen that the heat generation rate in the virtual wall acts as a heat source to balance the air convective heat flow Q_c and the anti-icing heat flow of the outer skin surface conducted from the electrical heaters Q_n. Therefore, the heat generation rate can be used to stand for the total effects of the impinging water droplets on the anti-icing surface, just like the heat and mass transfer processes of the runback water to take place in the virtual wall, as shown in Fig. 2. As the heat generation rate changes with the anti-icing surface temperature, the tightly coupled simulation of the electro-thermal anti-icing system can be carried out under icing conditions.

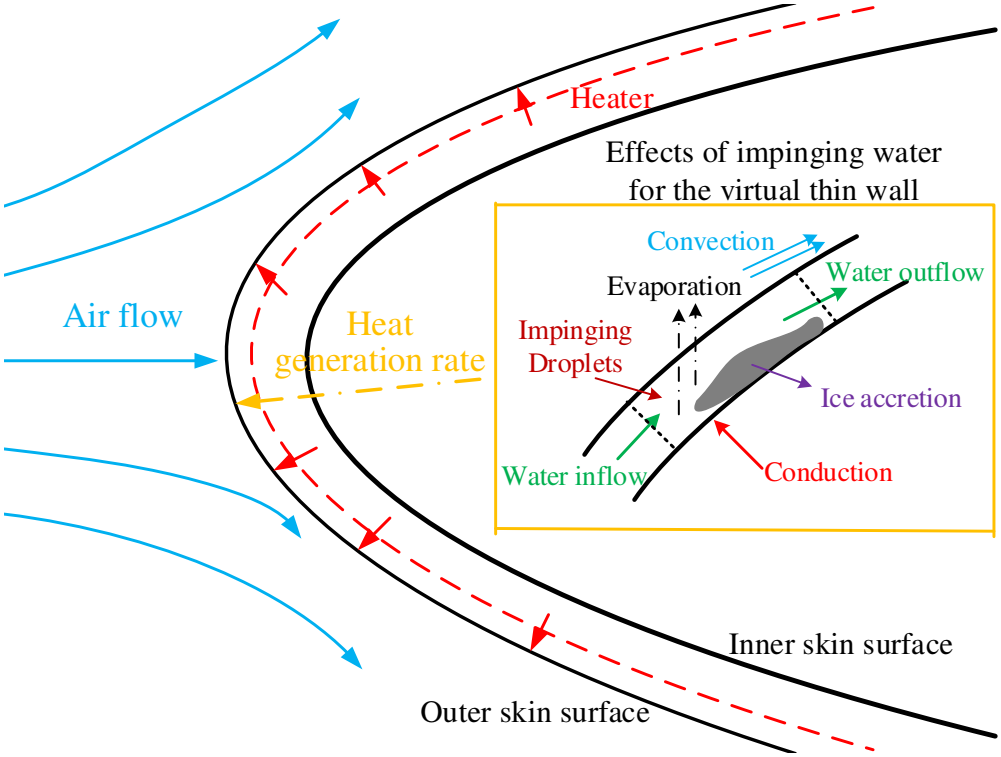

Fig. 2 Tight coupling method for an electro-thermal anti-icing system under icing conditions.

Obviously, the heat generation rate in the virtual wall is zero under the dry air condition. To obtain its value under the icing condition, thermodynamics of the runback water are firstly analyzed. According to the Messinger heat and mass transfer model [9], the mass and energy conservation equations of the runback water film on the anti-icing surface can be obtained [28]:

$$\dot{m}_{\mathrm{in}} + \dot{m}_{\mathrm{imp}} = \dot{m}_{\mathrm{evap}} + \dot{m}_{\mathrm{out}} + \dot{m}_{\mathrm{ice}} \tag{6}$$

$$Q_{\mathrm{imp}} + Q_{\mathrm{n}} + Q_{\mathrm{ice}} + Q_{\mathrm{in}} = Q_{\mathrm{c}} + Q_{\mathrm{evap}} + Q_{\mathrm{out}} \tag{7}$$

In traditional decoupled loose-coupling method, Q_{c} is obtained with the convective heat transfer coefficient under the isothermal wall boundary condition. In this work, Eq. (7) is combined Eq. (5), and the following equation can be obtained:

$$S \cdot H \cdot \Delta s = Q_{\mathrm{imp}} + Q_{\mathrm{ice}} - Q_{\mathrm{evap}} + Q_{\mathrm{in}} - Q_{\mathrm{out}} \tag{8}$$

Therefore, Q_{c} does not need to be calculated separately from the conjugate heat transfer, and the air convective heat transfer coefficient would be updated automatically. Moreover, the heat generation rate in a control volume (CV) of the virtual wall can be calculated by solving the tight-coupling heat and mass transfer model of Eq. (6) and Eq. (8).

In the equations above, the impinging water flow rate $\dot{m}_{\mathrm{imp}}$ can be obtained by the following equation [24]:

$$\dot{m}_{\mathrm{imp}} = \beta \cdot U_{\infty} \cdot LWC \cdot \Delta s \tag{9}$$

where LWC is the liquid water content.

The heat flow of the impinging water Q_{imp} is composed of the enthalpy and the kinetic energy of the water droplets, as expressed as:

$$Q_{\mathrm{imp}} = \dot{m}_{\mathrm{imp}} \cdot \left[\frac{U_{\infty}^2}{2} + c_{p,\mathrm{w}} \cdot (T_{\infty} - T_{\mathrm{ref}}) \right] \tag{10}$$

When the electrical heating power is insufficient for anti-icing, the runback water film on the surface would release latent heat and freeze into ice. After all the water is frozen, the ice temperature would be further reduced, releasing sensible heat. Therefore, the heat flow of the frozen water Q_{ice} is obtained by:

$$Q_{\mathrm{ice}} = \dot{m}_{\mathrm{ice}} \cdot \left[i_{\mathrm{ls}} + c_{p,\mathrm{ice}} \cdot (T_{\mathrm{ref}} - T_{\mathrm{s}}) \right] \tag{11}$$

When the air flows over the wet surface, the water evaporative heat flow Q_{evap} can be calculated by:

$$Q_{\mathrm{evap}} = \dot{m}_{\mathrm{evap}} \cdot i_{\mathrm{lv}} \tag{12}$$

The evaporative mass flow rate $\dot{m}_{\mathrm{evap}}$ is determined by the Chilton-Colburn analogy theory, as expressed as [23]:

$$\dot{m}_{\mathrm{evap}} = \Delta s \cdot \frac{h_{\mathrm{s}}}{c_{p,\mathrm{air}}} \cdot \left(\frac{Pr}{Sc}\right)^{2/3} \cdot \frac{\mathrm{M_v}}{\mathrm{M_{air}}} \cdot \left[\frac{p_{\mathrm{v,sat}}(T_{\mathrm{s}}) - p_{\mathrm{v,e}}}{p_{\mathrm{e}} - p_{\mathrm{v,e}}}\right] \tag{13}$$

where $p_{\mathrm{v,sat}}(T_{\mathrm{s}})$ is the saturated evaporative pressure at the local surface temperature. The convective heat transfer coefficient h_{s} is obtained by the convective heat flow and the temperature difference between the surface temperature and the reference temperature:

$$h_{\mathrm{s}} = \frac{Q_{\mathrm{c}}}{\left(T_{\mathrm{s}} - T_{\mathrm{ad}}\right) \cdot \Delta s} \tag{14}$$

With the water film flow from the stagnation point to the upper and lower anti-icing surfaces under the air shear stress, the heat flows carried by the runback water flow rates entering the current CV $\dot{m}_{\mathrm{in}}$ and flowing out of the CV $\dot{m}_{\mathrm{out}}$ are Q_{in} and Q_{out}, respectively. They could be calculated by

$$Q_{\mathrm{in}} = \dot{m}_{\mathrm{in}} \cdot c_{p,\mathrm{w}} \cdot (T_{\mathrm{in}} - T_{\mathrm{ref}}) \tag{15}$$

$$Q_{\mathrm{out}} = \dot{m}_{\mathrm{out}} \cdot c_{p,\mathrm{w}} \cdot (T_{\mathrm{s}} - T_{\mathrm{ref}}) \tag{16}$$

Since all the liquid water in CV would run back outwards in the Messinger model, the water flow rate entering the current CV is equal to the value flowing out of the upstream CV. In addition, the mass flow rate of runback water entering the stagnation point shall be equal to zero [16]. Therefore, the calculation of runback water flow is initiated at the stagnation point, and is performed from this point backwards along either side so that $\dot{m}_{\mathrm{in}}$ is a known quantity at each location.

The solid-liquid phase state of the runback water in the CV is directly related to the freezing point. According to the constraint, the solution of the new heat and mass transfer model for the heat generation rate can be divided into three conditions: at the freezing point, above the freezing point and below the freezing point.

Water solidification is assumed to happen over the small temperature range from T_{ref} to $T_{\mathrm{ref}}+\Delta T$, and ΔT is an artificial temperature range between water and ice phases [16, 21]. Therefore, if the CV temperature T_s is in the range of 273.15 K to 273.15 K+ΔT, it is considered to be at the freezing point, and part of the runback water freezes in to ice. In this condition, the freezing fraction f is defined as the ratio of the ice quality to the total water in the CV [26]:

$$f = \frac{\dot{m}_{\mathrm{ice}}}{\dot{m}_{\mathrm{in}} + \dot{m}_{\mathrm{imp}} - \dot{m}_{\mathrm{evap}}} \tag{17}$$

Based on LEWICE [16] and Domingos [21], the freezing fraction is related to the artificial temperature range ΔT, as expressed below.

$$f = 1 - \frac{T_s - T_{\text{ref}}}{\Delta T} \tag{18}$$

From Eq. (17) and Eq. (18), it can be derived that:

$$\dot{m}_{ice} \cdot \Delta T = \left(\dot{m}_{\text{in}} + \dot{m}_{\text{imp}} - \dot{m}_{\text{evap}} \right) \cdot \left(T_{\text{ref}} - T_s + \Delta T \right) \tag{19}$$

By solving Eq. (6), Eq. (8), and Eq. (19), the heat generation rate at the freezing point can be obtained.

If $T_s > 273.15\ \text{K} + \Delta T$, the anti-icing surface temperature is higher than freezing point, and there is no ice in the current CV. The conservation equations to be solved become:

$$\dot{m}_{\text{in}} + \dot{m}_{\text{imp}} = \dot{m}_{\text{evap}} + \dot{m}_{\text{out}} \tag{20}$$

$$S \cdot H \cdot \Delta s = Q_{\text{imp}} - Q_{\text{evap}} + Q_{\text{in}} - Q_{\text{out}} \tag{21}$$

If $T_s < 273.15$ K, the anti-icing surface temperature is lower than the freezing point, and all the runback water in the CV is frozen. The mass and energy conservation equations below are solved.

$$\dot{m}_{\text{in}} + \dot{m}_{\text{imp}} = \dot{m}_{\text{evap}} + \dot{m}_{\text{ice}} \tag{22}$$

$$S \cdot H \cdot \Delta s = Q_{\text{imp}} + Q_{\text{ice}} - Q_{\text{evap}} + Q_{\text{in}} \tag{23}$$

2.2. Solution procedure

The electro-thermal anti-icing simulation based on the tight-coupling method is implemented by the commercial CFD software ANSYS FLUENT - 18.1 with its user-defined functions (UDFs) [27], and the solution procedure is shown in Fig. 3.

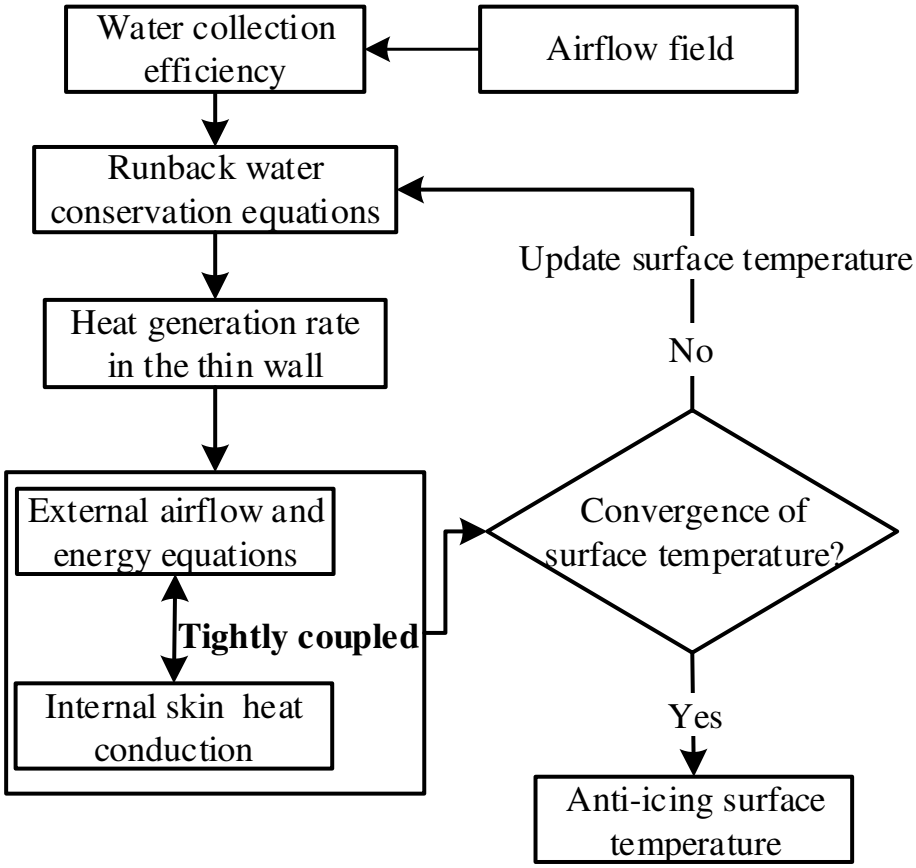

Fig. 3 Flow chart of anti-icing simulation based on tight coupling method.

Based on the fact that the super-cooled water droplets in the cloud have a very low volume fraction (about 10^{-6}) and small diameters (around 20 μm), the external air-droplet two-phase flow is usually considered one-way coupled [29], and the air flow field is independent from the droplet motion. In addition, it is assumed that there is no heat and mass transfer between the droplets and the surrounding air [12], and the impingement characteristics of the water droplets are slightly affected by the anti-icing surface temperature. Therefore, the air flow field for water droplet motion and the calculation of local water collection efficiency are both separated from the fluid-solid coupling heat transfer analysis, and the collection efficiency is then sent to the conservation equations of the runback water film, as shown in Fig. 3. The impingement characteristics can be obtained by Lagrangian method [30] or Eulerian method [31]. The Lagrangian method tracks each droplet's trajectory in the air flow, while the Eulerian one treats water droplets as a continuous medium and solves conservation equations of mass and momentum to obtain the droplet volume fraction and velocity fields. As these two methods are mature and the precisions can meet the anti-icing requirements, both will not be explained in detail here.

The external airflow field around the anti-icing surface is obtained by solving the Reynolds-averaged Navier-Stokes (RANS) equations. The exact value of a parameter is divided into two terms for the RANS equations: the mean component and the fluctuating component. Then, the continuity and momentum equations can be expressed as [27]:

$$\frac{\partial \rho}{\partial t}+\frac{\partial}{x_i}\left(\rho u_i\right)=0 \tag{24}$$

$$\frac{\partial}{\partial t}\left(\rho u_i\right)+\frac{\partial}{\partial x_j}\left(\rho u_i u_j\right)=-\frac{\partial p}{\partial x_i}+\frac{\partial}{\partial x_j}\left[\mu\left(\frac{\partial u_i}{\partial x_j}+\frac{\partial u_j}{\partial x_i}-\frac{2}{3}\delta_{ij}\frac{\partial u_l}{\partial x_l}\right)\right]+\frac{\partial}{\partial x_j}\left(-\rho\overline{u_i' u_j'}\right) \tag{25}$$

It can seen that the Reynolds stress, $-\rho\overline{u_i' u_j'}$, must be modeled in order to close Eq. 25. Currently, various turbulent models have been developed to solve the Reynolds stress. The one-equation Spalart-Allmaras (S-A) turbulence model, which is recommended by FENSAP-ICE software for good wall-bounded flow results, is utilized in the present work.

The temperature field in the fluid domain is obtained by the following energy equation:

$$\frac{\partial}{\partial t}\left(\rho E\right)+\frac{\partial}{\partial x_i}\left[u_i\left(\rho E+p\right)\right]=\frac{\partial}{\partial x_j}\left[\left(k+\frac{c_p\mu}{Pr}\right)\frac{\partial T}{\partial x_j}\right]+\frac{\partial}{\partial x_j}\left[u_i\left(\mu+\mu_t\right)\left(\frac{\partial u_i}{\partial x_j}+\frac{\partial u_j}{\partial x_i}-\frac{2}{3}\delta_{ij}\frac{\partial u_l}{\partial x_l}\right)\right]+S_h \tag{26}$$

Where the total energy E is expressed as:

$$E=h-\frac{p}{\rho}+\frac{U^2}{2} \tag{27}$$

Considering the effect of temperature on gas properties, air is set as an ideal gas whose thermal conductivity and viscosity are also regarded to change with temperature. Correspondingly, the boundary condition of pressure far field is used for the air flow inlet. In the solid domain, the energy equation becomes:

$$\frac{\partial}{\partial t}\left(\rho h\right)=\nabla(k\nabla T)+S_h \tag{28}$$

Therefore, with a coupled wall thermal boundary condition for the fluid-solid interface of the outer skin surface, the energy equations of both external air flow and internal multi-layered solid skin domains can be solved simultaneously including the heat generation and heat conduction in the coupled thin wall. The heat generation rate is obtained by solving the tight-coupling heat and mass transfer model of the runback water film. Then, the tightly

coupled energy equations can be solved simultaneously with the RANS equations by the finite volume solver of FLUENT.

Generally, during the tight-coupling iteration process of the thermal anti-icing simulation, the surface temperature T_s and the convective heat flow Q_c are extracted from the tightly coupled fluid-solid solution to update the convective heat transfer coefficient and the water evaporation rate. Meanwhile, according to the anti-icing surface temperature, the conservation equations of the runback water are solved under the different water-phase states to obtain the heat generation rate, as shown in Fig. 3. The heat generation rate is added to the tightly coupled fluid-solid calculation, and then a new temperature field is obtained for the next iteration. The surface temperature is considered to be the final solution when surface temperature variation before and after an iteration step satisfies convergence requirement.

3. Geometry and conditions

In order to verify the tight-coupling method, an electro-thermal anti-icing system of NACA 0012 airfoil is selected from open literature. The experiments of this system were performed by Al-Khalil [6] to validate ANTICE code at the NASA Lewis Research Center. Geometric models of the solid skin and its surrounding air flow domain are built together with fine structured grids, as shown in Fig. 4. The normal distance of the first layer grid outside the anti-icing surface is very small with the maximum y^+ of about 0.3, which meets the requirement of S-A model for solving boundary layer flow [27]. As heat conduction equation is insensitive to grid aspect ratio and has a relatively low requirement for mesh, a coarser one is competent for the solid skin, which is not shown in Fig. 4. Grid independence has be checked before the analyses of the results. The multi-layered skin consists of six layers, and the thicknesses and the physical properties of the materials are listed in Table 1. The heating layer is arranged near the outer skin surface to benefit the energy for anti-icing, and minimize the heat leakage to inner side of the skin. Therefore, the adiabatic boundary condition is used for the inner skin surface.

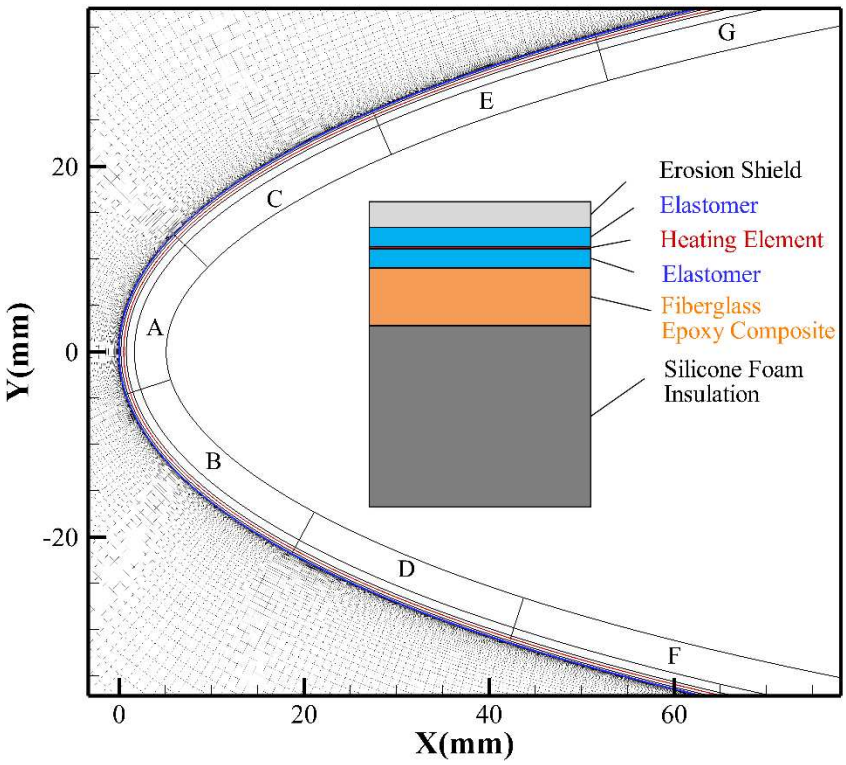

Fig. 4 Geometry and heaters of the electro-thermal anti-icing system.

Table 1 Material properties of the multi-layered skin [6].

Material	Conductivity (W/(mK))	Density (kg/m^3)	C_p (J/(kgK))	Thickness (mm)
Heating Element(alloy 90)	41.018	8906.26	385.112	0.0127
Erision Shield(SS 301 HH)	16.269	8025.25	502.32	0.2032
Elastomer(COX 4300)	0.256	1383.99	1255.8	0.2794
Fiberglass/Epoxy Composite	0.294	1794.07	1569.75	0.889
Silicone Foam Insulation	0.121	648.75	1130.22	3.429

The electrical heating layer is arranged around the leading edge of the NACA 0012 airfoil, and consists of seven heating elements. The power density of each element can be individually controlled. Due to manufacturing difficulties, the seven heating elements are not symmetrically installed, but are offset from the leading edge [6]. The start and end positions of each element are presented in Table 2, where the dimensionless surface distance s/c=0 means the leading edge point and the value of the upper surface is positive. Case22A and Case22B are chosen from the experiments for

the anti-icing simulation based on the tight-coupling method. The two cases share the same boundary conditions for the external air flow and super-cooled water droplets: the flight velocity is 44.7 m/s with angle of attack of 0°, the ambient temperature is -7.6 °C, *LWC* is 0.78 g/m^3, and the median volumetric diameter of water droplet is 20 μm. The heating power densities of those two cases are different, and heat fluxes of the heating elements for each case are also listed in Table 2.

Table 2 Position and heat flux of electrical heater [6].

Heating element	Start_s/c	End_s/c	Heat flux (kW/m^2)	
			Case 22A	Case 22B
F	-0.1024	-0.0607	9.92	2.635
D	-0.0607	-0.0329	10.23	2.945
B	-0.0329	-0.0051	32.5	4.03
A	-0.0051	0.0157	46.5	4.805
C	0.0157	0.0435	18.6	2.945
E	0.0435	0.0713	6.98	3.41
G	0.0713	0.1129	10.24	2.325

4. Results and Discussion

4.1. Results under dry air conditions

The tight-coupling calculations are firstly carried out under dry air conditions without considering the impingement of the super-cooled water droplets, and the effects of the virtual wall on the heat transfer characteristics are studied. The aluminum with the thermal conductivity of 200 W/(mK) is used for the virtual wall, while the wall thickness is set to be 0 μm and 10 μm, respectively. Since the heat generation rate is zero for dry air conditions, the heat flux equality condition of Eq. (2) is guaranteed no matter how thick the virtual wall is. In addition, when the wall thickness is 0 μm, the temperature equality condition of Eq. (1) is satisfied, and the tight-coupling results under the dry air conditions are considered accurate. Fig. 5 shows the temperature and heat flux distributions on the surfaces of the virtual wall under the two thicknesses. Since the heat fluxes of the electrical heaters in Case22A and Case22B are for icing conditions, the dry air results are just for comparisons and analyses without considering the temperature

limits of the skin materials. It can be seen that the surface temperature and heat flux of Case22A are much higher than those of Case22B due to the larger heating power. When the wall thickness H=10 μm, the temperature deviations between the fluid and solid boundaries at the interface are very small. In addition, the temperature and heat flux results of H=10 μm are consistent with those of H=0 μm for both dry air cases. According to Eq. (3), the maximum temperature difference between the two surfaces of the thin wall is only about 0.0025 K for H=10 μm, so the heat transfer characteristics under the two thickness conditions agree very well. The effects of the virtual wall on the conjugate heat transfer can be neglect with this small thermal resistance setting, and the thickness of 10 μm and the thermal conductivity of 200 W/(mK) are suitable for the tight-coupling simulations under icing conditions.

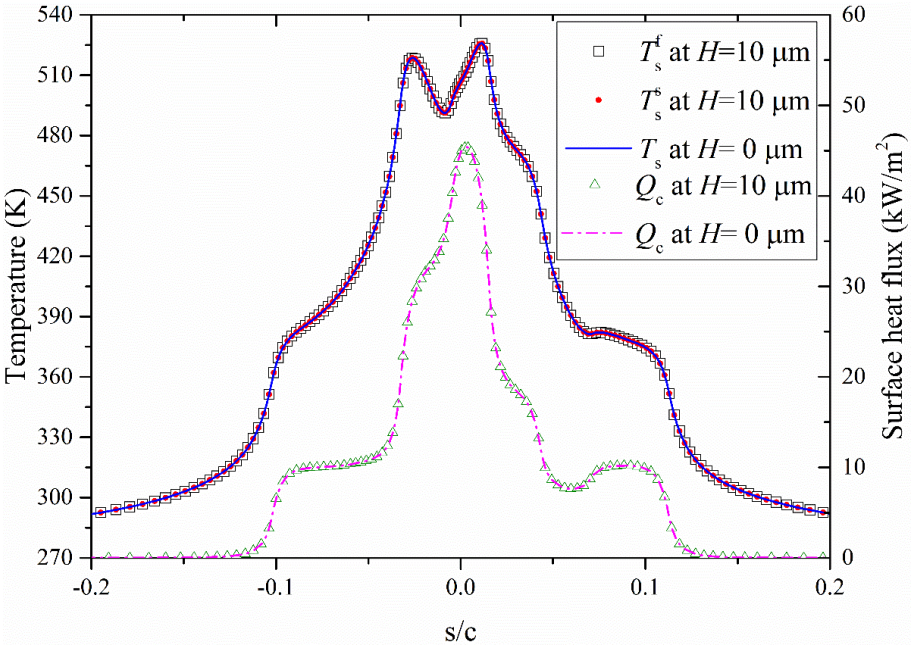

(a) Case22A

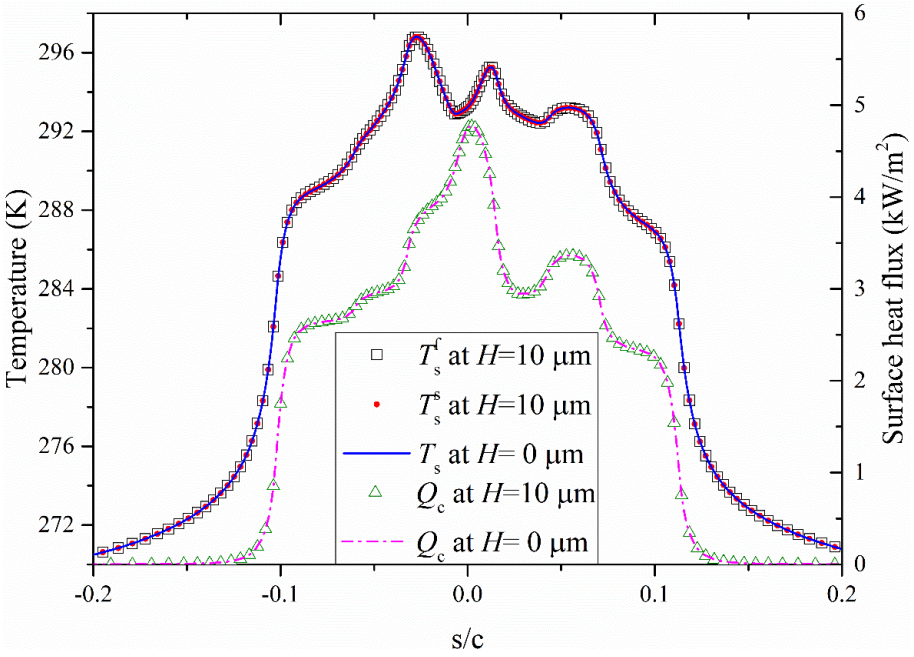

(B) Case22B

Fig. 5 Anti-icing surface temperature and heat flux under dry air conditions.

The convective heat transfer coefficients under the dry air conditions are obtained by Eq. (14) from the tight-coupling solutions, and they are compared with the results under the isothermal wall boundary conditions, as shown in Fig. 6. The surface temperature can be higher than 500 K under dry air conditions, while the values of Case22A and Case22B from literature data [6] are around 320 K and 280 K, respectively. Therefore, the isothermal wall temperatures of 280 K, 320 K and 500 K are used for the airfoil surface.

It can be seen that the convective heat transfer coefficients under the different temperature distributions show good agreement near the leading edge, even though the values at the high temperature of 500K and the dry air temperature of Case22A are a little higher at the stagnation point. In the downstream area, the curves at the different isothermal wall temperatures have the same trend that the convective heat transfer coefficients increase at the laminar-turbulent transition region and then gradually decrease behind this region. The value is lower when the isothermal temperature is higher, which may be caused by the heat absorption of the boundary layer from the wall surface. When the isothermal wall temperature is higher, more heat is transfer to the air boundary layer from the upstream surface, leading to the weaker cooling capacity and lower convective heat transfer coefficient of air in the downstream area.

On the other hand, the convective heat transfer coefficients at the non-isothermal temperatures of Case22A and Case22B fluctuates frequently on the downstream surfaces, and the deviations are obvious. In addition, as the

dimensionless surface distance s/c increases out of the protected area, the convective heat transfer coefficients obtained by the tight-coupling method decrease to zero. It just means no heat transfer occurs as shown in Fig. 5, and the convective heat flow Q_c in Eq. (14) is zero rather than the physical convective heat transfer coefficient being zero.

In general, the convective heat transfer coefficient near the leading edge is slightly affected by the surface temperature and its distribution, whereas the value of the downstream turbulent zone changes greatly with the non-isothermal wall temperature. This phenomenon was also found in Ref. [26] where the calculation results were obtained based on the SST-kω turbulence model.

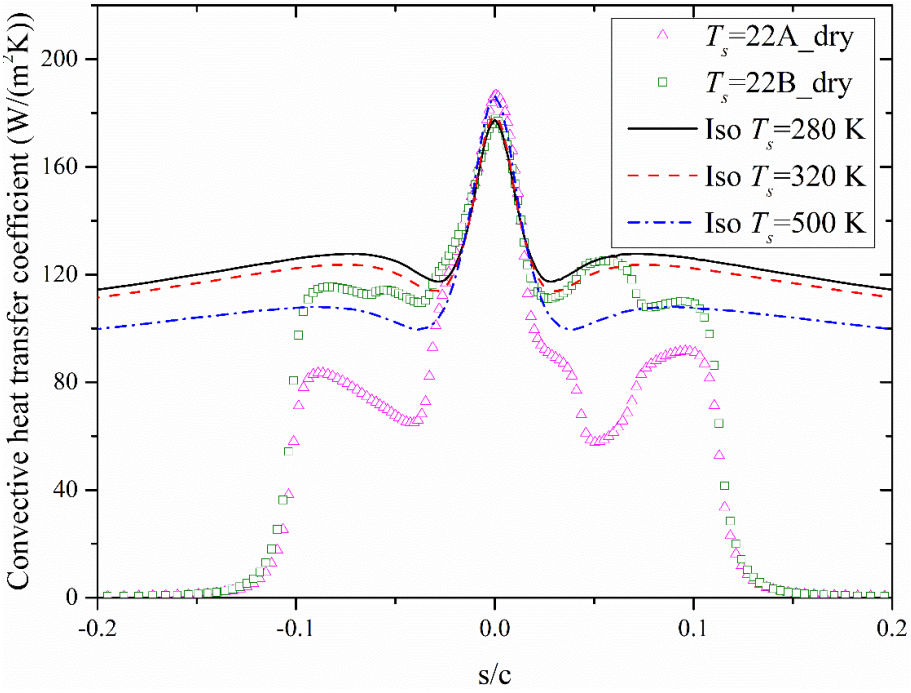

Fig. 6 Convective heat transfer coefficients with different surface temperatures.

The convective heat transfer coefficients at the isothermal temperatures are used as thermal boundary conditions of the outer skin surface to calculate the temperatures by the decoupled method, and the results are compared with the tight-coupling solutions under the dry air conditions, as shown in Fig 7. The temperature differences between the two coupling methods are small near the leading edge, and become obvious in the downstream area. The temperature drop rates obtained by the tight-coupling method are relatively low, and the temperatures in the unheated region are still high for both dry air cases. However, the values of the decoupled method decrease rapidly on the downstream surface, and reach the ambient temperature near the ends of the protected area. Hence, without updating convective heat

transfer coefficient, the decoupled loose-coupling method cannot predict accurate heat transfer characteristics away from the leading edge area.

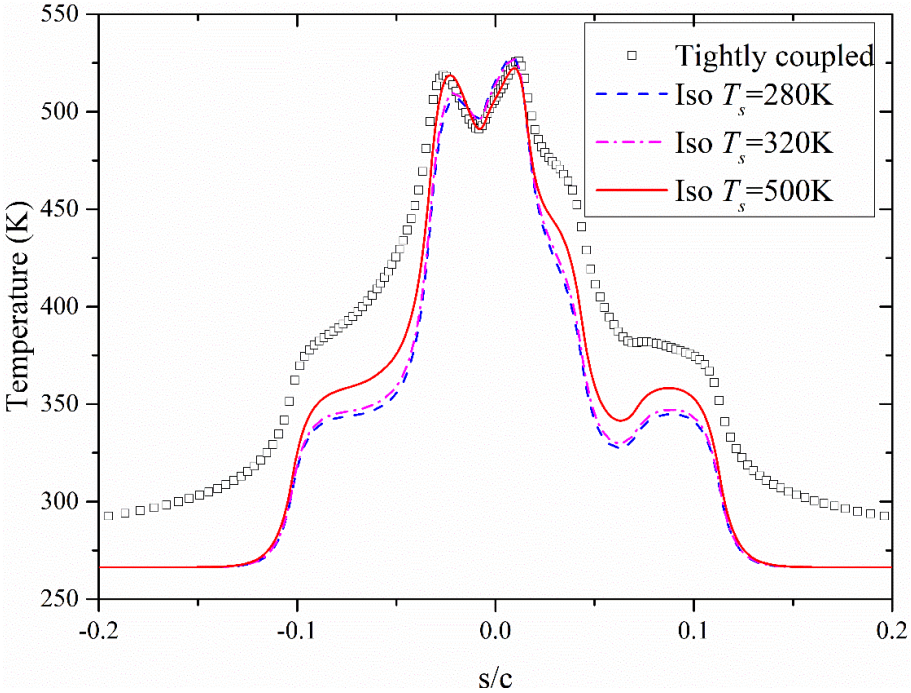

(a) Case22A

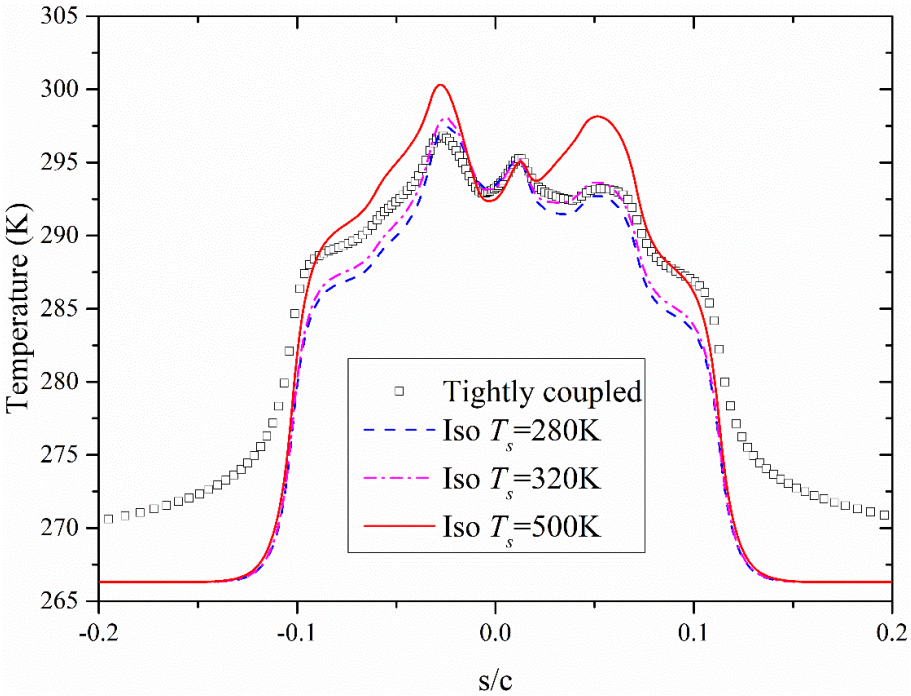

(b) Case22B

Fig. 7 Comparisons of temperature distributions based on different coupling methods.

4.2. Anti-icing results of Case22A

The airflow fields for water droplet motions are obtained under the surface conditions at the dry air tight-coupling temperatures and the isothermal temperatures. One-way coupled Eulerian method [32] is applied for the water droplet flow and surface impingement characteristics, and the local water droplet collection efficiencies at different surface temperatures are shown in Fig. 8. The results all reach their maxima at the stagnation point, and decrease to zero as the distance from the leading edge increases. The local collection efficiencies agree well with the calculation of Silva [33], and are almost unaffected by the surface temperature and its distribution, indicating that it is feasible and effective to separate the solutions of the water droplet motion and impingement characteristics from the tight-coupling heat transfer calculations.

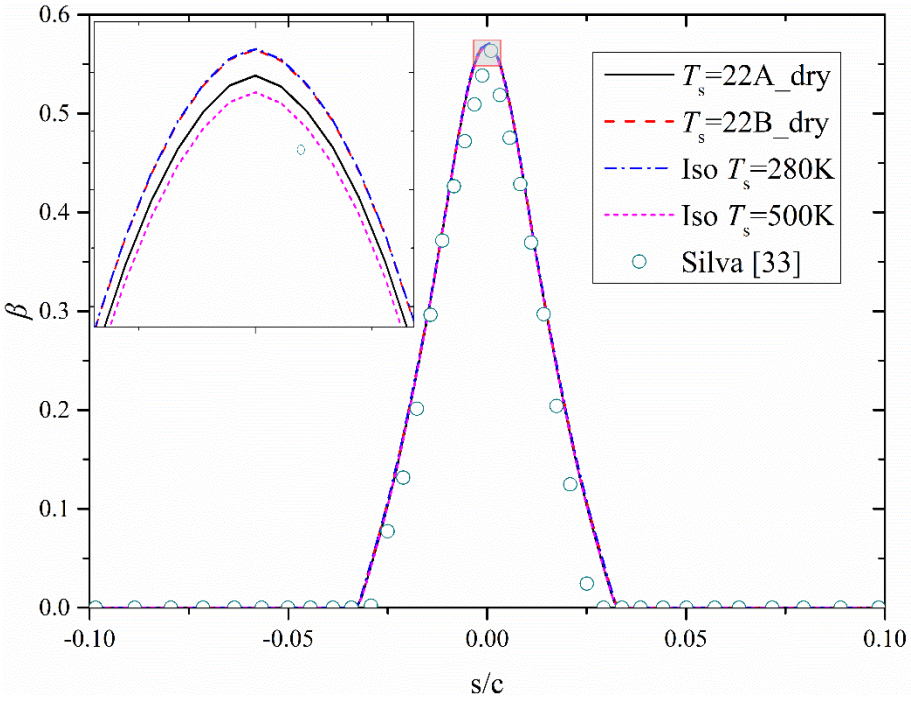

Fig. 8 Local collection efficiencies of different surface temperatures.

With the local collection efficiency on the anti-icing surface, tight-coupling simulations are carried out under the icing conditions. The electro-thermal anti-icing results are compared with those of the traditional decoupled loose-coupling method [28]. The convective heat transfer coefficients of the decoupled method are obtained at the isothermal surface temperatures, as shown in Fig. 6. The curve at the isothermal temperature of 320K is used for Case22A, while the value at 280K is used for Case22B. Neither of the convective heat transfer coefficients are updated during the decoupled iterative process of the internal solid skin heat conduction and the runback water heat transfer.

Fig. 9 and Fig. 10 present the distributions of runback water flux and anti-icing surface temperature for Case22A. The anti-icing results obtained by the tight-coupling method and the decoupled loose-coupling method also show good agreement near the airfoil leading edge, which also indicates that the convective heat transfer coefficient in this region is unaffected by surface temperature. Since the surface temperature of Case 22A is high due to large heating power, the impinging water is totally evaporated within the ice protected area. In addition, the runback water range is small, and locates just near the leading edge with the ends at about positions of s/c$\approx\pm$0.03. Therefore, the difference of the runback water flux between the two coupling methods is small, and the range obtained by the tight-coupling method is slightly larger. On the other hand, as the distance to the leading edge increases outside the runback water range, dry surface is formed with much higher surface temperature, and temperature deviation appears between the two coupling methods. The surface temperature calculated by the tight-coupling method is lower than that of the decoupled one in the protected area, but higher with lower drop rate in the unheated region. The surface temperature of the decoupled method drops rapidly to the ambient temperature when moving away from the protected area, which is the same with the situations under both dry air conditions.

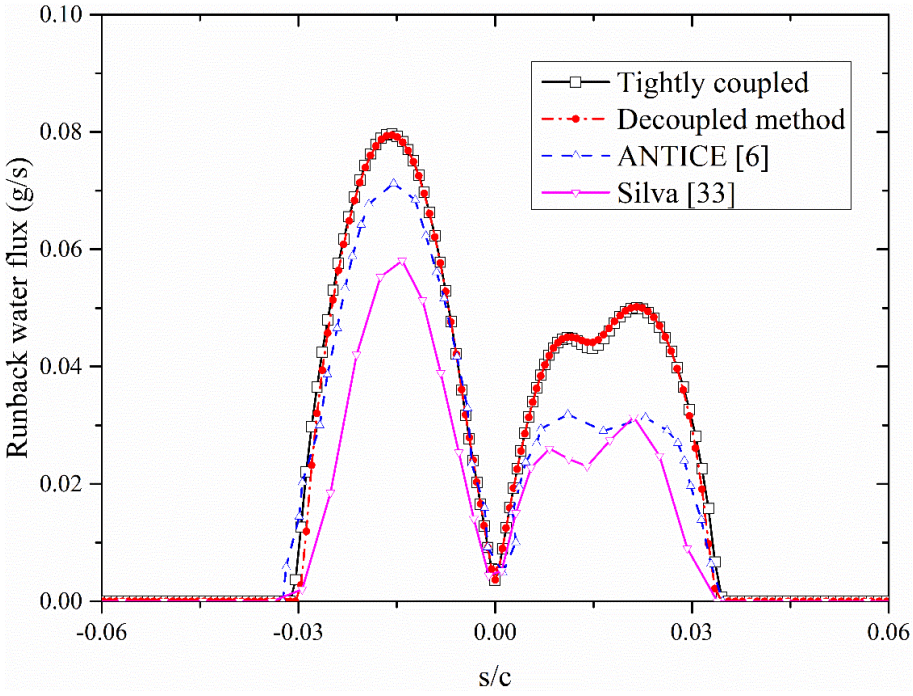

Fig. 9 Runback water flux for Case22A.

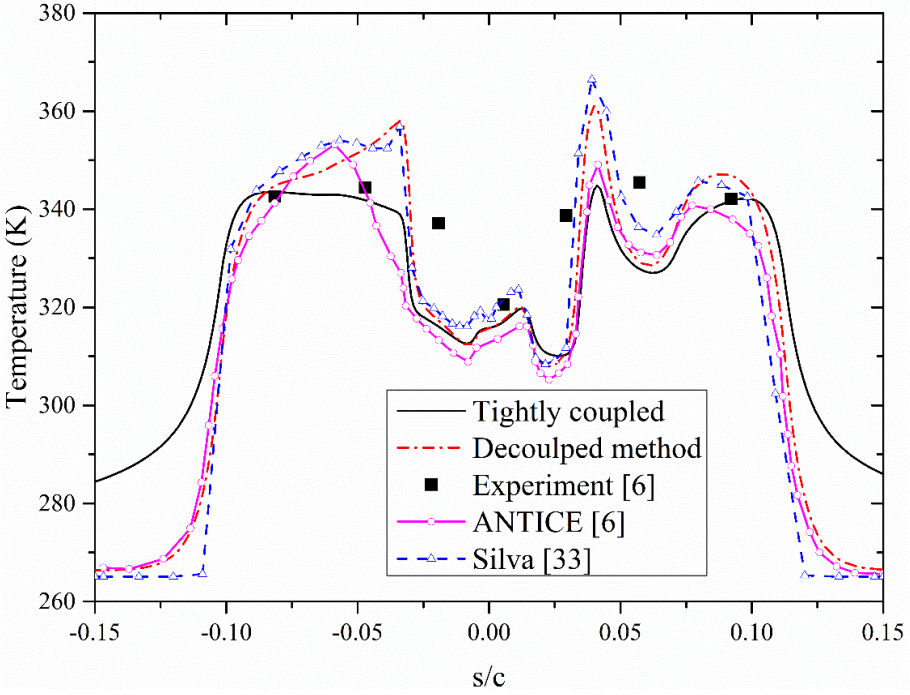

Fig. 10 Anti-icing surface temperature distribution for Case22A.

Since the fixed convection heat transfer coefficient is added in the same decoupled way to the heat and mass transfer model of the runback water film, the surface temperature obtained by the loose-coupling method matches better with the results of ANTICE [6] and Silva [33]. However, the temperature deviation between the predicted result of the tight-coupling method and the experiment data is acceptable and comparable to other numerical simulation results. In addition, the tight-coupling method can model the temperature drop characteristics found under the dry air conditions in the unheated region. Therefore, the effectiveness and advantage of the tight-coupling method are verified for the simulations under evaporative anti-icing conditions.

4.3. Anti-icing results of Case22B

Case22B is a running-wet anti-icing condition, and the runback water flux and surface temperature are shown in Fig. 11 and Fig. 12, respectively. Compared with the results of Case22A, the surface temperature of Case22B is much lower, while the runback water range is wider. The runback water flux is also low at the leading edge, and increases as it moves backwards gathering more droplets in the droplet impingement range. The value then decreases gradually from the impingement limits, and the drop rate becomes much larger in the unheated region where ice ridge is formed. Meanwhile, the surface temperature changes with the electrical heating power in the protected area, and drops quickly

to the freezing point outside this area. The temperature then keeps at the freezing point when it moves backwards, until all the runback water freezes into ice.

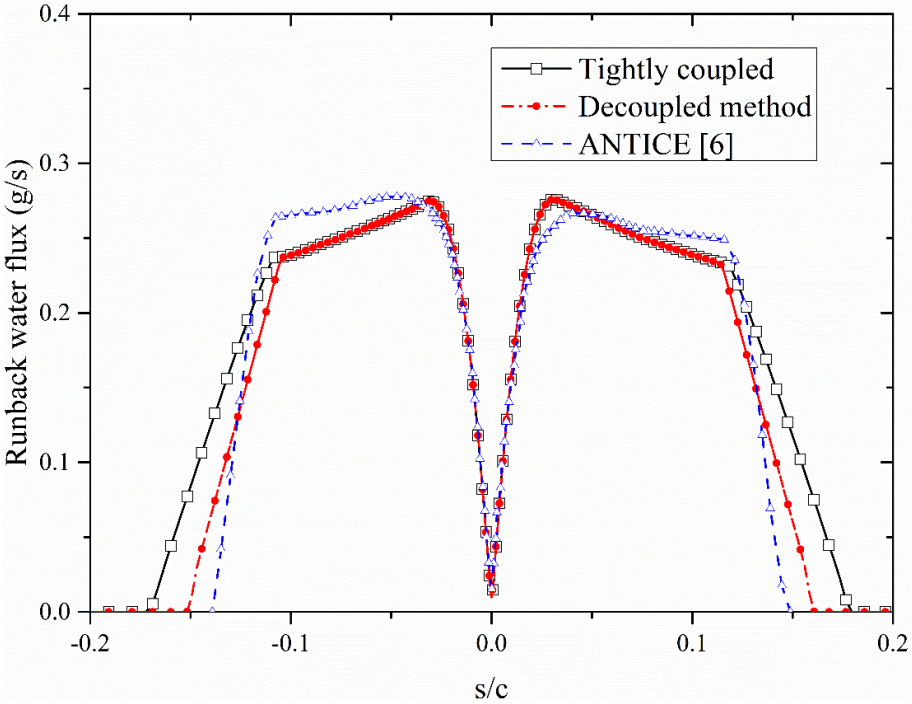

Fig. 11 Runback water flux for Case22B.

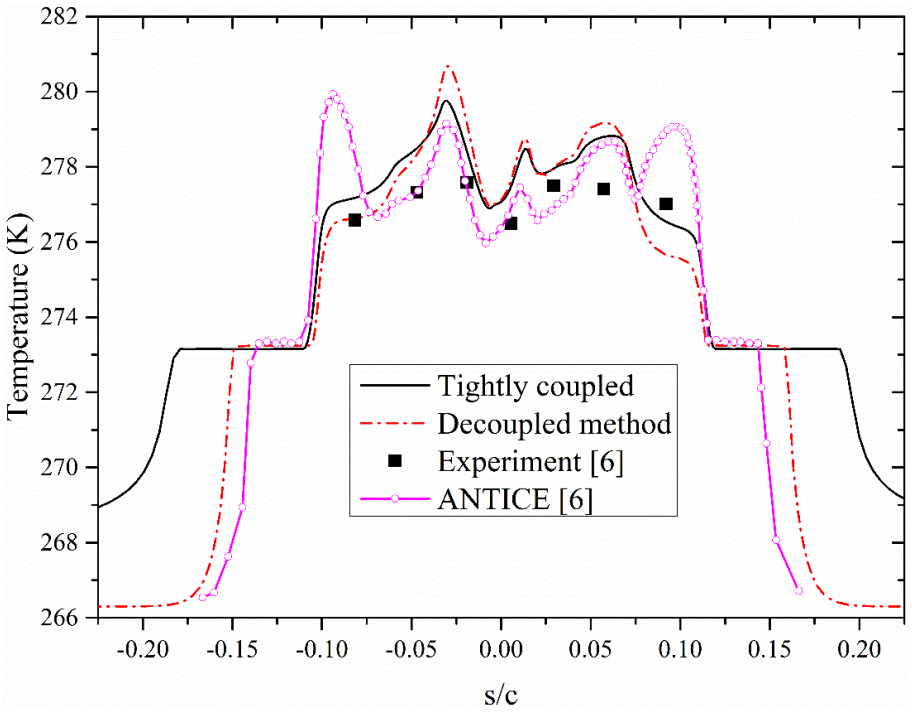

Fig. 12 Anti-icing surface temperature distribution for Case22B.

It can also be found that the curves of the runback water flux and surface temperature obtained by the tight-coupling and decoupled loose-coupling methods have good consistency near the leading edge. The temperature deviation occurs as the dimensionless surface distance increases, and the surface temperature curve of the tight-coupling method is moderate with smaller fluctuation amplitude. When the runback water flows out of the protected area to freeze, the runback water range and the surface area at the freezing point obtained by the decoupled method are quite closer to the results of ANTICE [6], and their temperatures are both reduced quickly from the freezing point to the ambient value after all water freezes. Those runback range and surface area predicted by the tight-coupling method are larger than those of ANTICE, and the maximum deviation is about 0.035 in the dimensionless surface distance. The surface temperature also keeps higher in the unprotected area, and needs a longer distance to drop.

From the comparison of the loosely coupled methodology with updated convective heat transfer coefficient and the decoupled one based on the use of the isothermal wall boundary condition in Ref. [21], the surface area at the temperature of 273.15 K obtained by the decoupled methodology was smaller than that of the coupled one, and the temperature drop rate was higher. Those situations are the same with the comparison result of Case22B in this paper. Therefore, the anti-icing simulation results obtained by the tight-coupling method may be more believable. In addition, there is an acceptable agreement between the predicted temperature and the experiment data for Case22B, indicating the feasibility of the tight-coupling method for the running-wet anti-icing simulation.

4.4. Analysis and discussion

The tight-coupling results of surface temperatures and convective heat transfer coefficients under the icing conditions are analyzed together in Fig. 13. Compared with the dry air temperatures in Fig. 5, the addition of the runback water film on the anti-icing surface leads to lower surface temperatures and different temperature distributions. The convective heat transfer coefficients and their distributions also change a lot under the icing conditions. Although the surface temperature of Case22A is much higher than that of Case22B, the difference of the convective heat transfer coefficients is not obvious near the leading edge, which is the same with the situation under the dry air conditions. In this region, the influences of the surface temperature on the boundary layer are still not expanded with laminar flow, so the deviations of the air properties and the convective heat transfer coefficient are limited.

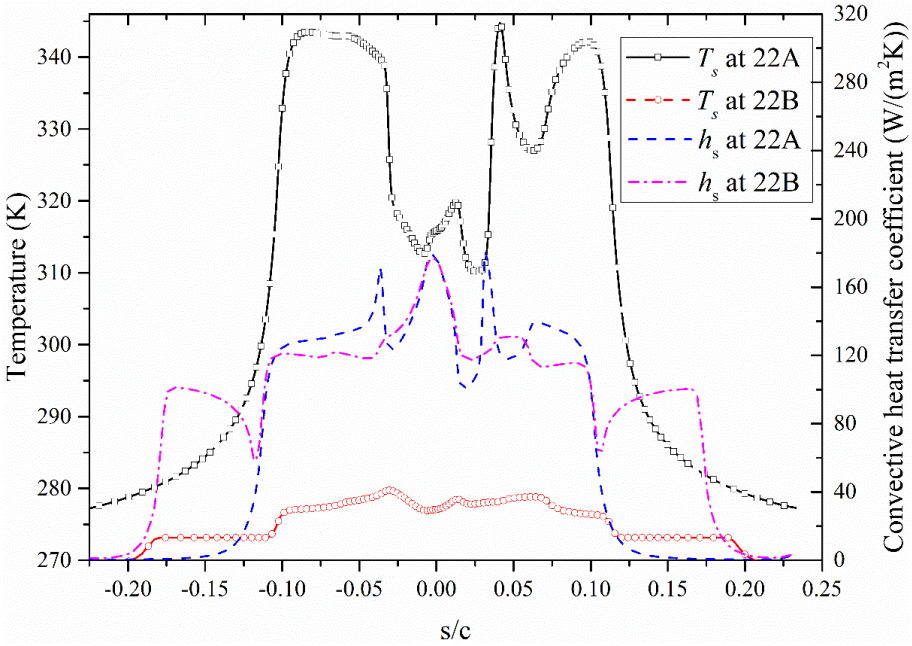

Fig. 13 Anti-icing surface temperature and convective heat transfer coefficient.

It can be seen from Fig. 13 that the convective heat transfer coefficient of Case22A increases to a peak near the positions of s/c≈±0.04 where the temperatures rapidly rise due to the disappearance of the runback water film on the surface. With the peak of the convective heat transfer coefficient, the predicted surface temperature is lower than that of the decoupled method. This phenomenon of convective heat transfer coefficient rise is also observed by Morency [19]. The reason is not only the boundary layer development but also the surface temperature distribution. If the surface temperature increases along the direction of air flow, the air temperature in the upstream boundary layer is lower than that in the downstream location. When this lower temperature air flows through the higher temperature downstream surface, the temperature difference between the surface and the boundary layer is enlarged compared with isothermal wall condition. Therefore, the air can take more heat away from downstream surface, and the convective heat transfer coefficient increases. On the other hand, if the temperature of the upstream boundary layer is higher, the cooling capacity of air is weakened. When it flows through the wall with a relatively low temperature, the dissipation heat flux is less than that of the isothermal wall, and the convective heat transfer coefficient decreases. These results can be found at the edges of the protected area for both cases and at the limits of the runback water range for Case22B, as shown in Fig. 13. Those effects of temperature distributions on convective heat transfer coefficients can also be analyzed and obtained by the boundary layer integration theory [34].

Moreover, when the surface temperature distribution is more complex, coupled with the effects of air property change and boundary layer transition in turbulence flows, the relationship between convective heat transfer coefficient and surface temperature are more complicated with many fluctuations in the curves of the convective heat transfer coefficients. For example, when the surface temperature of Case22B keeps at the freezing point in the runback water icing range, the influence of lower upstream temperature is gradually reduced, and the convective heat transfer coefficient increases until surface temperature changes. In addition, compared with the decoupled results, the downstream surface temperatures obtained by the tight-coupling method drop more slowly outside the heated area, and keep above the ambient value in larger regions for all the dry air and icing conditions. This may be caused by higher upstream temperature. Since these downstream temperature phenomena under dry air conditions are similar with that of Case22A, the detailed analyses are carried out only for the anti-icing solutions.

Fig. 14 and Fig. 15 show the temperature contours of Case22A and Case22B obtained by the two coupling methods. It can be seen clearly that the skin temperatures of the decoupled loose-coupling simulations rapidly decrease to the ambient temperature at the edges of the protected area for Case22A and at the limits of the runback water range for Case22B, while the temperatures obtained by the tight-coupling method drop very slowly within the downstream skin. The temperature of the boundary layer rises due to heat transfer from the anti-icing surface, and the high temperature air would act like a “protected layer” to reduce the heat dissipation from downstream surface. Therefore, the downstream surface temperature drops slowly, and keeps at higher value in large area. As the surface temperature gradually decreases to the boundary layer temperature, the surface heat flux then declines to zero. This phenomenon is well captured by the tight-coupling method as shown in Fig. 14 and Fig. 15. The loose-coupling method, however, cannot simulate it. The convective heat transfer coefficient used in the decoupled calculation does not change with the surface temperature, and the heat flux conducted from upstream skin is quickly taken away by the surrounding low temperature air. As a result, the decoupled skin temperature drops rapidly to the ambient value.

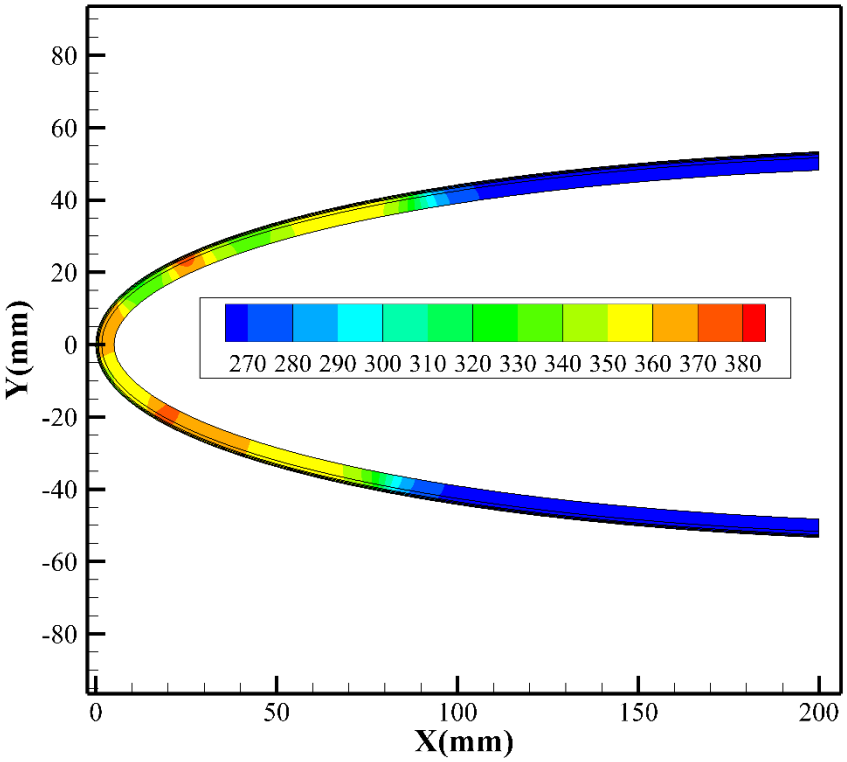

(a) Result of the decoupled loose-coupling method

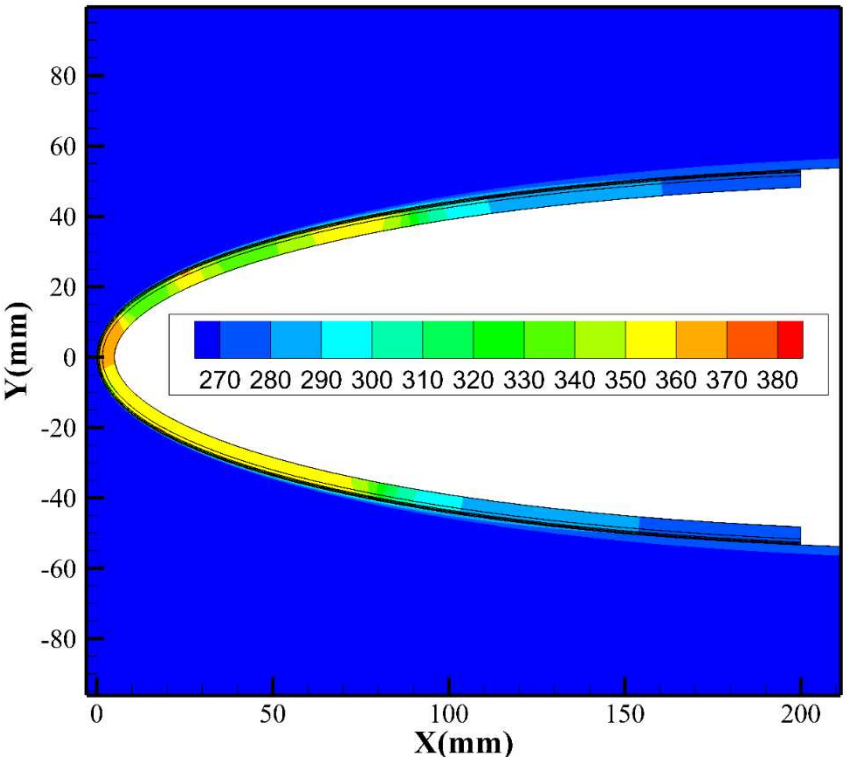

(b) Result of the tight-coupling method

Fig. 14 Contour of temperature (K) for Case22A.

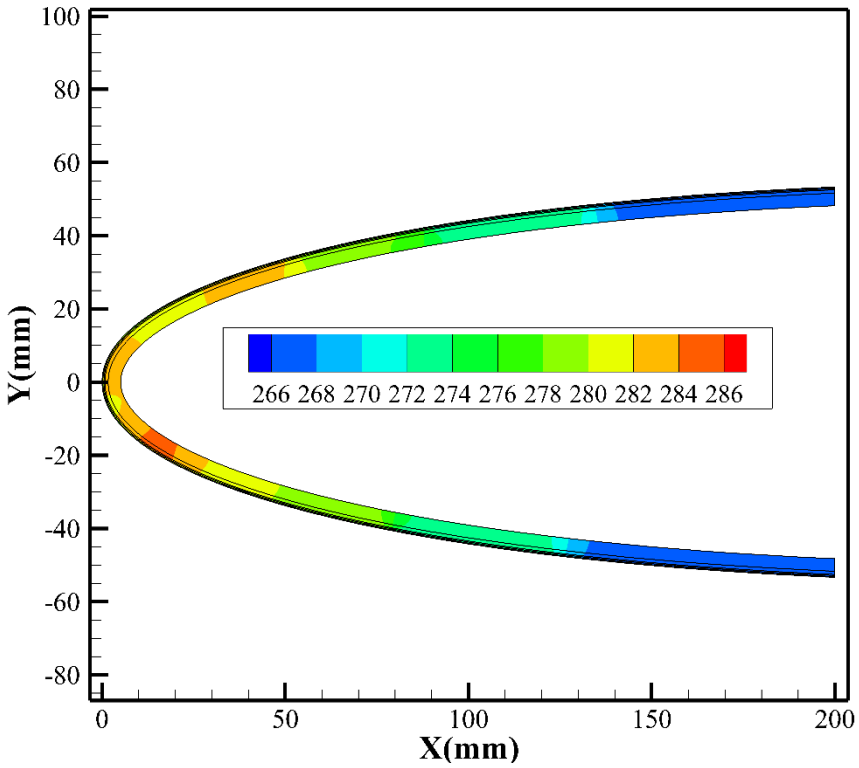

(a) Result of the decoupled loose-coupling method

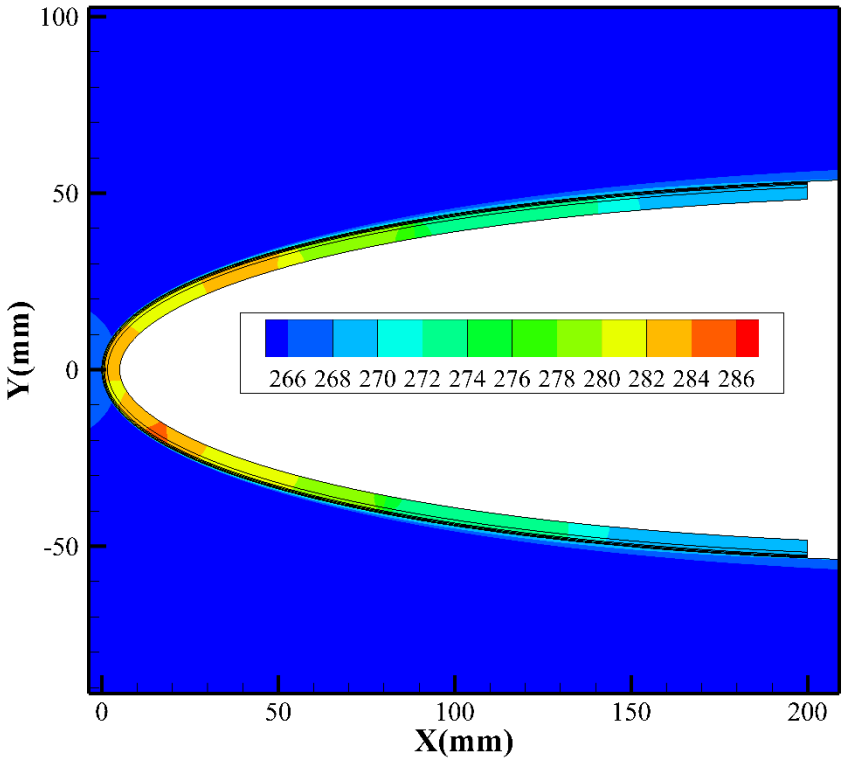

(b) Result of the tight-coupling method

Fig. 15 Contour of temperature (K) for Case22B.

5. Conclusion

With the tightly coupled mass and heat transfer model of the runback water in the virtual thin wall, the tight-coupling method for aircraft thermal anti-icing simulations under icing conditions is established. Numerical calculations are carried out on the electro-thermal anti-icing system of NACA0012 airfoil under the dry air and icing conditions. It is found that the convective heat transfer coefficient near the leading edge is slightly affected by surface temperature and its distribution. However, the non-isothermal surface temperature has a great influence on the downstream heat transfer characteristics, which in turn affects the prediction of the thermal anti-icing system.

Compared with the traditional decoupled loose-coupling method, the robust tight-coupling method updates convective heat transfer coefficient according to surface temperature automatically, and predicts higher anti-icing surface temperature with lower drop rate on the downstream surfaces, which is considered more reasonable based on the dry air results and the phenomenon observed in the literature. In addition, the anti-icing surface temperatures obtained by the tight-coupling method are in acceptable agreement with the experiment data, and are comparable to the simulation results in the literature, which verifies the feasibility and effectiveness of the model.

The main difference of the predicted results between the traditional decoupled loose-coupling method and the present tight-coupling method lies in the downstream region. Since the experiment monitors all locate around the leading edge, both coupling methods can obtain acceptable results. More experiment data is needed for further verification of the tight-coupling anti-icing method in the region away from the leading edge.

Conflict of interest

Author declares that there is no conflict of interest.

Acknowledgements

This work was supported by the National Numerical Wind Tunnel Project (No. NNW2019ZT2-A07), the National Natural Science Foundation of China (No. 51806008), and the National Science and Technology Major Project (No. 2017-VIII-0003-0114). The support provided by China Scholarship Council (CSC) during the visit of Xiaobin Shen at the University of Leeds is also acknowledged.

References

[1] Y. Du, Y. Gui, C. Xiao, X. Yi, Investigation on heat transfer characteristics of aircraft icing including runback water, International Journal of Heat and Mass Transfer. 53 (2010) 3702-3707. DOI: 10.1016/j.ijheatmasstransfer.2010.04.021.

[2] Y. Cao, J. Huang, J. Yin, Numerical simulation of three-dimensional ice accretion on an aircraft wing, International Journal of Heat and Mass Transfer. 92 (2016) 34-54. DOI: 10.1016/j.ijheatmasstransfer.2015.08.027.

[3] X. Zhang, J. Min, X. Wu, Model for aircraft icing with consideration of property-variable rime ice, International Journal of Heat and Mass Transfer. 97 (2016) 185-190. DOI: 10.1016/j.ijheatmasstransfer.2016.01.065.

[4] M. Papadakis, S.H. Wong, H.W. Yeong, S.C. Wong, Icing tests of a wing model with a hot-air ice protection system, in: AIAA Atmospheric and Space Environments Conference, AIAA-2010-7833, 2010.

[5] L. Ding, S. Chang, S. Yang, and M. Leng, Study on heating strategies of nose cone electrothermal anti-icing, Journal of Aircraft. 55(3)(2018) 1310-1314. DOI: 10.2514/1.C034639.

[6] K.M. Al-Khalil, C. Horvath, D.R. Miller, W.B. Wright, Validation of NASA thermal ice protection computer codes. III - The validation of ANTICE, in: 35th Aerospace Sciences Meeting and Exhibit, AIAA-97-0051, 1997.

[7] W. Dong, M. Zheng, J. Zhu, G. Lei, Calculation and analysis of runback water flow on anti-icing airfoil surface, Journal of Aircraft. 53(6) (2016) 1597-1605. DOI: 10.2514/1.C033637.

[8] S.K. Thomas, R.P. Cassoni, C.D. MacArthur, Aircraft Anti-Icing and De-Icing Techniques and Modeling, Journal of Aircraft. 33(5) (1996) 841–854. DOI: 10.2514/3.47027.

[9] B.L. Messinger, Equilibrium temperature of an unheated icing surface as a function of airspeed, Journal of the Aeronautical Sciences. 20(1) (1953) 29-42. DOI: 10.2514/8.2520.

[10] T.G. Myers, J.P.F. Charpin, A mathematical model for atmospheric ice accretion and water flow on a cold surface, International Journal of Heat and Mass Transfer 47 (2004) 5483-5500. DOI: 10.1016/j.ijheatmasstransfer.2004.06.037.

[11] M. Pourbagian, W.G. Habashi, Aero-thermal optimization of in-flight electro-thermal ice protection systems in transient de-icing mode, International Journal of Heat and Fluid Flow, 54 (2015) 167–182. DOI: 10.1016/j.ijheatfluidflow.2015.05.012.

[12] M.P. Barzi, 3D conjugate heat transfer simulation of aircraft hot-air anti-icing systmes, M.D. Dissertation, Mechanical Engineering Dept., McGill Univ., Montreal, HA, 2005.

[13] J. Hua, F. Kong, H.H.T. Liu, Unsteady thermodynamic computational fluid dynamics simulations of aircraft wing anti-icing operation, Journal of Aircraft. 44(4) (2007) 1113-1117. DOI: 10.2514/1.24122.

[14] M. Papadakis, S.H. Wong, S.C. Wong, CFD analysis of a wing with a bleed air ice protection system, in: 5th AIAA Atmospheric and Space Environments Conference, AIAA-2013-2935, 2013.

[15] F. Petrosino, P. Mormile, M. Musto, N. Bianco, G. Mingione, G. Rotondo, CFD analysis of a coupled bleed air and electrothermal icing protection system, in: 9th AIAA Atmospheric and Space Environments Conference, AIAA-2017-3756, 2017.

[16] W.B. Wright, User manual for the NASA Glenn ice accretion code LEWICE version 2.2.2, NASA-CR-2002-211793, 2002.

[17] T. Reid, G.S. Baruzzi, W.G. Habashi, FENSAP-ICE: unsteady conjugate heat transfer simulation of electrothermal de-icing, Journal of Aircraft. 49(4) (2012) 1101-1109. DOI: 10.2514/1.C031607.

[18] R. Chauvin, P. Villedieu, P. Trontin, A robust coupling algorithm applied to thermal ice protection system unsteady modeling, in: 6th AIAA Atmospheric and Space Environments Conference – AVIATION, 2014.

[19] F. Morency, F. Tezok, I. Paraschivoiu, Anti-Icing System Simulation Using CANICE, Journal of Aircraft. 36(6) (1999) 999-1006. DOI: 10.2514/2.2541.

[20] O. Harireche, P. Verdin, C.P. Thompson, D.W. Hammond, Explicit finite volume modeling of aircraft anti-icing and de-icing, Journal of Aircraft. 45(6) (2008) 1924-1936. DOI: 10.2514/1.34855.

[21] R.H. Domingos, M. Papadakis, A.O. Zamora, Computational Methodology for Bleed Air Ice Protection System Parametric Analysis, in: AIAA Atmospheric and Space Environments Conference, AIAA-2010-7834, 2010.

[22] M.P. Barzi, Multidisciplinary optimization of in-flight electro-thermal ice protection systems, Ph.D. Dissertation, Mechanical Engineering Dept., McGill Univ., Montreal, HA, 2014.

[23] X. Bu, G. Lin, J. Yu, S. Yang, X. Song, Numerical simulation of an airfoil electrothermal anti-icing system, Proc IMechE Part G: Journal of Aerospace Engineering. 227(10) (2013) 1608-1622. DOI: 10.2514/6.2009-4250.

[24] Z.D. Mu, G.P. Lin, X.B. Shen, X.Q. Bu, Y. Zhou, Numerical simulation of unsteady conjugate heat transfer of electro-thermal deicing process, International Journal of Aerospace Engineering. (2018) 1-16. DOI: 10.1155/2018/5362541.

[25] F. Morency, F. Tezok, I. Paraschivoiu, Heat and mass transfer in the case of anti-icing system simulation, Journal of Aircraft. 37(6) (2000) 245–252. DOI: 10.2514/2.2613.

[26] R.H. Domingos, Computational methodoloty for bleed air ice protection system parametric analysis, M.D. dissertation, Aerospace Engineering Dept., Wichita State Univ., Wichita, KS, 2010.

[27] Ansys, Ansys FLUENT User's Guide, Software Package, Ver. 18.1, Ansys Inc., 2018.

[28] X. Shen, X. Liu, G. Lin, X. Bu, D. Wen, Effects of Anisotropic Composite Skin on Electro-thermal Anti-icing System, Proc IMechE Part G: J Aerospace Engineering. 233(14) (2019) 5403-5413. DOI: 10.1177/0954410019845980.

[29] E. Iuliano, V. Brandi, G. Mingione, C.D. Nicola, R. Tognaccini, Water impingement prediction on multi-element airfoils by means of Eulerian and Lagrangian approach with viscous and inviscid air flow, in: 44th AIAA Aerospace Sciences Meeting and Exhibit, AIAA-2006-1270, 2006.

[30] S. Wang, E. Loth, Droplet Impact Efficiency on Aerodynamic Surfaces with a Globally Eulerian/Locally Lagrangian Method, Journal of Aircraft. 54(1) (2017) 104-113. DOI: 10.2514/1.C032968

[31] S. Wirogo, S. Srirambhatla, An Eulerian method to calculate the collection efficiency on two and three dimensional bodies, in: 41st Aerospace Science Meeting and Exhibit, AIAA-2003-1073, 2003.

[32] X. Shen, G. Lin, S. Yang, H. Wang, Eulerian method for droplets impingement calculation, in: Proceedings of 48th SAFE Symposium, 2011.

[33] G.A.L. Silva, O.M. Sivares, E.J.G.J. Zerbini, Numerical simulation of airfoil thermal anti-ice operation part 2: Implementation and results, Journal of Aircraft. 44(2) (2007) pp. 635-641. DOI: 10.2514/1.24922.

[34] W.M. Kays, M.E. Crawford, B. Weigand, Convective heat and mass transfer (Fourth Edition), McGraw Hill Higher Education, 2005. (ISBN: 0071238298)